

Article

Analysis of Wind Turbine Wake Dynamics by a Gaussian-Core Vortex Lattice Technique

Apurva Baruah and Fernando Ponta * 

Department of Mechanical Engineering-Engineering Mechanics, Michigan Technological University, Houghton, MI 49931, USA; baruah@mtu.edu

* Correspondence: flponta@mtu.edu

Abstract: The development and deployment of the next generation of wind energy systems calls for simulation tools that model the entire wind farm while balancing accuracy and computational cost. A full-system wind farm simulation must consider the atmospheric inflow, the wakes and consequent response of the multiple turbines, and the implementation of the appropriate farm-collective control strategies that optimize the entire wind farm's output. In this article, we present a novel vortex lattice model that enables the effective representation of the complex vortex wake dynamics of the turbines in a farm subject to transient inflow conditions. This work extends the capabilities of our multi-physics suite, CODEF, to include the capability to simulate the wakes and the high-fidelity aeroelastic response of multiple turbines in a wind farm. Herein, we compare the results of our GVLM technique with the LiDAR measurements obtained at Sandia National Laboratories' SWiFT facility. The comparison shows remarkable similarities between the simulation and field measurements of the wake velocity. These similarities demonstrate our model's capabilities in capturing the entire wake of a wind turbine at a significantly reduced computational cost as compared to other techniques.

Keywords: vortex methods; wind farm simulation; wind turbine wake; vortex dynamics; wake analyses; Lagrangian methods; vortex lattice



Citation: Baruah, A.; Ponta, F. Analysis of Wind Turbine Wake Dynamics by a Gaussian-Core Vortex Lattice Technique. *Dynamics* **2024**, *4*, 97–118. <https://doi.org/10.3390/dynamics4010006>

Academic Editor: Christos Volos

Received: 4 December 2023

Revised: 9 January 2024

Accepted: 17 January 2024

Published: 1 February 2024



Copyright: © 2024 by the authors. Licensee MDPI, Basel, Switzerland. This article is an open access article distributed under the terms and conditions of the Creative Commons Attribution (CC BY) license (<https://creativecommons.org/licenses/by/4.0/>).

1. Introduction

Wind power science has seen tremendous development and growth over the last 40 years. Advancements in the design, manufacturing, installation, and operation of wind turbines have enabled the rapid commercial deployment of wind power generation systems. The large-scale commercial deployment of wind turbines has led to a decline in the levelized cost of energy (LCOE) [1]. This reduction in the LCOE has primarily been driven by advancements in wind turbine technology, particularly the increased hub height, rotor diameter, and, consequently, rated power. These economies-of-scale factors have been augmented by innovations in wind turbine blades. Modern blades are sophisticated aerodynamic structures, manufactured using highly advanced materials and processes. The blades today also possess the modular capabilities of incorporating several after-market upgrades with relative ease. These developments have ensured that today's wind turbines are able to maximize power production while keeping costs low.

However, even with these advancements, some of the classical problems still remain. Especially the well-known “square-cube law” associated with the upscaling of wind turbines. For a particular wind speed, the mass of the rotor scales with the cube of the rotor radius (the *volume*) whereas the power generated scales with the square (rotor area). Moreover, even though the increasing costs can be balanced elsewhere in this large wind energy conversion system, future advancements are bound by this law.

Maximizing the energy extraction process for the future calls for a holistic view of all aspects of a wind power system. Developmental efforts need to be broadened to include not just single turbines but also the optimization of the collective wind farm and,

moreover, the fleet of wind farms connected to the overall electricity grid. This calls for comprehensive analyses of the various multi-scale phenomena involved, beginning from the local flow and response of the turbines to the complex flows through a wind farm, and, finally, the regional and global weather phenomena. To this end, the IEA Wind TCP has articulated the *Grand Challenges* that position wind power as the primary form of electricity, providing one-third to (potentially) one-half of the demand, as reported by Dykes et al. [2] and Veers et al. [3]. The first grand challenge emphasizes the need for an improved understanding of the physics of the complex flows within wind farms. The simplification of the complex physics involved has allowed for the proliferation of wind power plants; however, there are major gaps in our thorough understanding of all the underlying phenomena. This understanding is critical for ensuring the optimal design and operation of the next generation of wind farms.

Fundamental to the design of a wind farm is the understanding of the evolution, interaction, and consequent impact, of the wakes of turbines in the farm. Intuitively, the presence of the wakes of upstream turbines significantly impacts the power production of downstream turbines. These wakes also lead to varying loads on the downstream turbine. The complex wakes vary according to the size and type of turbine, and the prevalent wind and turbine operating conditions. Hence, their analyses are crucial in order to maximize energy production and lower the capital and operational costs.

Studying the wakes at scale, in “test” wind farms is impossible because of the uncontrollable, transient, and spatially varying nature of wind. Computational models and simulations are indispensable tools available for the understanding of wind turbine wakes for the design and development of wind farms.

Several models have been developed for the analyses of the wind turbine wakes, from simplified techniques [4] to the various types of CFD techniques, such as Reynolds-Averaged Navier–Stokes (RANS) [5–7] and Large Eddy Simulation (LES) (such as Ellip-Sys3D [8], PALM [9], SOWFA [10], and NALU [11,12]). All of these models have varying degrees of fidelity and associated computational costs. Typically, higher-fidelity models tend to require increasing amounts of computational resources leading up to Direct Numerical Simulation (DNS) codes [13], which are practically intractable for wind-farm simulations. While LES has been a favored candidate in contemporary research [14,15], it still requires a large amount of computational power (albeit far less than DNS).

One family of techniques that can fill this gap is vortex methods, which for several decades have been formulated for wind turbines and other types of open-flow turbomachinery, such as propellers, helicopter rotors, and hydrokinetic turbines. These models are based on representations of the turbine blades and their wakes by assemblies of vortex filaments, or by a set of the so-called vortex “blobs”. More detailed descriptions of different alternatives for the vortex modeling approach can be found in Leishman [16], in particular when applied to helicopter rotors.

Vortex methods do not involve the large number of simplifications inherent to low-fidelity models, and, at the same time, do not require the large modeling and computational resources of conventional high-fidelity CFD-based techniques (LES). Belonging to the Lagrangian framework, vortex methods, in contrast to the Eulerian techniques, significantly reduces the computational requirements since the computations are performed only at the Lagrangian markers. These Lagrangian markers (or the nodes of the vortex filaments) are naturally tracked along their evolution exactly where they are, instead of the really large computational domain of conventional Eulerian techniques. These methods can compute the velocity field at any arbitrary location as a simple, independent post-processing operation. After a certain limit, the Eulerian (or grid-based) methods are completely ill-suited for such complex flows.

Focus of this Study

As we already discussed in the previous paragraphs, tremendous progress has been made in the design and development of a diverse set of modeling tools that individually

address the different multi-physics aspects of wind power systems. The structural dynamics of the turbine can be studied using reduced order models and modal analysis all the way up to complete 3D finite elements. The aeroelastic response of the blades can be studied using the models belonging to the BEM family (see Manwell et al. [17] and Burton et al. [18], among others), or 3D, coupled FSI codes.

However, the continued growth in the deployment of new wind energy systems rests on the successful integration of interlinked multi-scale physics. The coupling of the aero–elasto–inertial physics of an individual turbine with the farm flow models is an indispensable step for any coupled multi-physics modeling system. With such a system, other aspects of the wind farm dynamics, such as farm-collective control strategies involving different electro–mechanical components, the farm microgrid, and, ultimately, the overall grid dynamics, can then be successfully included. This *unified* modeling framework shall enable the development and deployment of future wind farms.

The comprehensive modeling system needs to have the capability to solve all the non-linear, coupled, physics involved at their appropriate spatial and temporal scales—using manageable computational resources. Thus, the challenge is to develop a coupled, multi-physics, transient modeling system that can provide solutions of appropriate fidelity at a reasonable computational cost.

Various modeling techniques integrate a subset of the different physics of wind energy systems, at varying levels of abstraction and fidelity. It is the aim of the current endeavor to expand on a system based on a multi-physics unified paradigm building on the existing Common ODE Framework (CODEF) technique introduced in Ponta et al. [19]. Leveraging the capabilities of Lagrangian, vortex lattice-based methods, this article describes the development and validation of a novel free vortex lattice technique called the Gaussian-core Vortex Lattice Model (GVLM). A further step in the development of wind turbine modeling systems, the GVLM accurately represents the complex dynamics of wind turbine wake evolution, capturing features of wake structure and meandering that are extremely challenging and computationally expensive to represent by the existing models mentioned above.

Seamlessly integrating with CODEF, the new GVLM module expands CODEF's capabilities to accurately represent the collective farm flow, and the turbine-to-turbine interaction, with a high level of fidelity and a moderate computational cost. Thus, the GVLM introduces into CODEF a feature that is essential for representing the collective farm dynamics in simulations run under different operational scenarios. The CODEF-GVLM combination provides researchers in the wind energy discipline with a tool that allows the testing and implementation of innovative control strategies for the farm collective. This would ultimately translate into an optimization of the entire farm's efficiency and reliability as a power generation plant.

2. The Common ODE Framework (CODEF)

In this section, we shall discuss CODEF, the multi-physics virtual test environment for wind turbines whose capabilities have been expanded by the body of work presented here. We shall also briefly describe its underlying structural and aerodynamic modules.

CODEF is an adaptive, variable-time step/variable-order ODE solver for wind turbine dynamics. The modularity of this *common framework* allows for easy integration of all of the dynamic components of a wind turbine to solve a master ODE system. Aspects affecting the dynamics of the turbine, such as the rotor flow, blade structure, control system, and electro–mechanical device, can be added to the feedback system in the form of modules comprised their representative differential equations and modifications to the boundary conditions. CODEF thus is able to treat these modules individually while interfacing with them using a computationally efficient, non-linear, adaptive ODE routine. By monitoring the local truncation error at each time step, it integrates all of the different multi-physics aspects of the problem, improving the efficiency and ensuring the stability of the time-marching numerical scheme.

Such modularity supports the independent development of the existing modules, and, at the same time, promotes the expansion of CODEF's capabilities. CODEF is perfectly suited for seamlessly interconnecting the dynamics of an individual turbine with new modules intended for the farm-scale flow, the wind farm collective control system, and the intra-farm microgrid. Figure 1 is a flow-diagram of CODEF outlining the interrelations between the different modules along with the newly added capabilities to simulate wind farms.

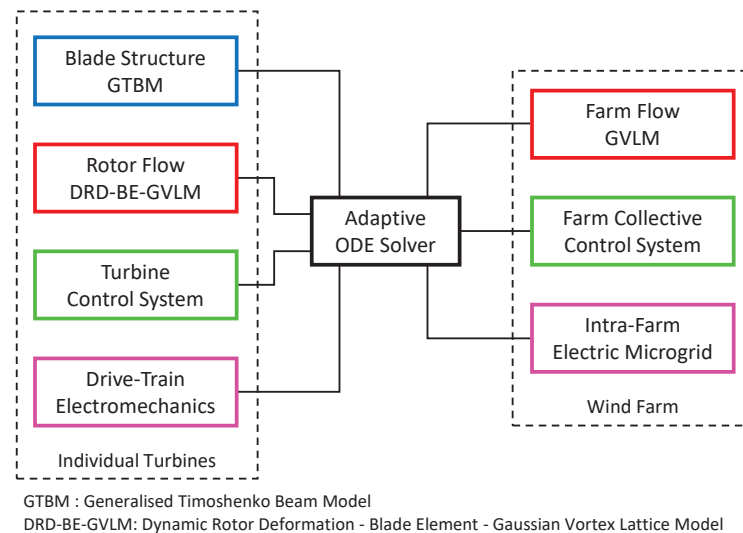


Figure 1. Common ODE Framework with expanded capabilities for farm simulations.

Dynamic Rotor Deformation—Blade Element Momentum (DRD-BEM)

We shall now briefly describe the novel member of the BEM model family, called the Dynamic Rotor Deformation—Blade Element Momentum model (DRD-BEM), introduced by Ponta et al. [19]. This model accounts for the aerodynamic effects of the misalignment of each blade section. It is achieved by the transformation of the velocity and force vectors across the different coordinate systems, from that of the free-stream wind to that of the blade section. These transformations are performed via a set of orthogonal matrices that account for all the misalignments—including those brought about by the deformation of the blade, mechanical inputs such as pitch and yaw, and even pre-conformed misalignments such as the pre-bend of the turbine blade.

The DRD-BEM is coupled with an advanced structural model that is based on a modified implementation of the Generalised Timoshenko Beam model (GTBM). A dimensional reduction method, GTBM has the same parameters as the traditional Timoshenko model and can work for complex beams that may have twisted or curved shapes. In this model, originally introduced by Hodges et al. [20,21], the beam section does not remain planar after deformation, and a 2D finite element mesh is used to interpolate the warping of the deformed section. A mathematical formulation is used to write the 3D strain energy in terms of the classical 1D Timoshenko model. Therefore, the complexity of the 3D model and geometry of the blades are reduced into a stiffness matrix for the corresponding 1D beam, which can then be solved along a reference line representing the beam's axis on the original configuration. This reference line can curve in any direction and hence follows the blade's deformation to its instantaneous configuration. Since the blade sections in their chord-normal, chord-wise, and span-wise directions stay aligned, an accurate tracking of the positions is possible even in the case of large deformations and rotations of the sections. The GTBM technique ensures a fully populated 6×6 symmetric stiffness matrix instead of only six stiffness coefficients obtained in the classical Timoshenko theory. The inertial properties are also dimensionally reduced to produce a 6×6 inertia matrix and all parameters, such as the angular, linear, centrifugal, and acceleration effects, are taken into account for a full 3D representation. Therefore, using the GTBM technique, we can

decouple a 3D nonlinear problem into a linear 2D analysis at the cross-sections and a nonlinear 1D unsteady beam problem, which, for the aeroelastic analysis, we solve at each time step using an advanced ODE algorithm (CODEF). Thus, the structural and aerodynamics modules are integrated and can be coupled with other modules within CODEF.

A detailed description of the implementation of the DRD-BEM model can be found in Ponta et al. [19] and the references therein. The DRD-BEM has been subsequently applied to the analysis of the aeroelastic dynamics of rotors undergoing rapid pitch-control actions to study the effect of fluctuations in wind conditions due to turbulent motions and to analyze the effects of blade-section misalignment on rotor cyclic loads. Ponta et al. [19] contains details about the specific implementation of GTBM and also includes the results of the DRD-BEM model applied to the analysis of the vibrational modes of composite laminated wind turbine blades, together with validation results against the works of Jonkman et al. [22] and Xudong et al. [23].

3. The Gaussian-Core Vortex Lattice Model

Many classical vortex lattice schemes that have been used for years are generally based on the Biot–Savart law to compute the swirling velocity induced by a single vortex filament in its surroundings (see Strickland et al. [24], Ponta and Jacovkis [25], Karamcheti [26], and Cottet and Koumoutsakos [27], among others). The Biot–Savart formulation is essentially an idealized model in which the velocity induced by a vortex filament of a finite length at any generic point P in its surrounding space is given by

$$\mathbf{V}^P = \mathbf{e} \frac{\Gamma}{4\pi h} (\cos \Theta_1 + \cos \Theta_2) \quad (1)$$

where, as indicated in Figure 2, Γ is the circulation of the vortex, h is the distance perpendicular to the filament to any generic point P in space, \mathbf{e} is the unit vector given by the cross product between the axis of the filament and the distance axis to that P point, and Θ_1 and Θ_2 are the internal angles between the axis of the filament and the distance axes to point P from each one of the filament's ends.

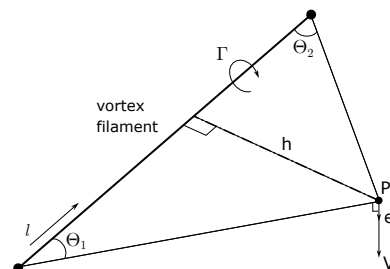


Figure 2. Velocity induced on a generic point in space by a vortex filament of finite length.

An inspection of Equation (1) indicates that, as a generic point in space moves closer to a Biot–Savart filament, the induced velocity at that point increases dramatically, to the extent that it becomes infinite if the point lies on the axis of the filament itself (i.e., when h becomes zero). This is completely unrealistic. In fact, in any real vortex, the velocity induced at a point located at the center of the vortex core is zero.

When a filament operates as part of an assembly in the context of a vortex lattice method, these unrealistically high velocities induced in the immediate vicinity of each individual filament will ultimately destabilize the mutual advection of all the filaments in the lattice. This ultimately leads to an absolutely chaotic advection pattern that has no resemblance to the actual evolution of the vortex wake structure.

An alternative representation of the vortex core behavior was proposed by Lamb [28] (Chap. XI, Art. 334a), and it is known as the “Lamb-Vortex Model” (see also Ponta [29], Batchelor [30], Hooker [31], Flór and van Heijst [32], and Trieling et al. [33] for more details about this model and its applications).

Based on an analogy with a classical solution of transient heat conduction in a homogeneous medium, the Lamb-Vortex Model provides a more realistic representation of the radial distribution of the swirling velocity via the adoption of a Gaussian radial distribution for the vorticity in the vortex core. In Lamb's model, the vorticity evolves over time, spreading radially into the flow domain, in a manner analogous to temperature in the two-dimensional diffusion of heat from a point-concentrated heat source emerging instantaneously at time zero. This Gaussian vorticity distribution is given as a function of the radial distance from the vortex axis r and the time t since the moment of the emergence of the vortex singularity:

$$\omega(r, t) = \frac{\Gamma}{4 \pi \nu t} (e^{-r^2/4\nu t}) \quad (2)$$

where ν is the kinematic viscosity of the fluid media. The corresponding magnitude of the induced swirling velocity along the radial distance is given by

$$V(r, t) = \frac{\Gamma}{2 \pi r} (1 - e^{-r^2/4\nu t}). \quad (3)$$

At any instant in time, V is maximum for a radius r_c such that

$$\frac{r_c^2}{4 \nu t} = 1.26 \Rightarrow r_c^2 = 5.04 \nu t \Rightarrow r_c = 2.245 \sqrt{\nu t} \quad (4)$$

while the peak vorticity at the center of the vortex core at any instant in time is

$$\omega_p = \frac{\Gamma}{4 \pi \nu t}. \quad (5)$$

The r_c parameter can be interpreted as the measure of an *equivalent core radius* for the vortex. The r_c radius expands as the vortex evolves in time via the vorticity diffusion process, at a rate controlled by the kinematic viscosity of the fluid media ν . The same diffusion process controls the rate of decay of the peak vorticity ω_p .

Substituting Equation (4) into Equation (3), an expression for the swirling induced velocity in terms of r_c can be obtained

$$V(r, t) = \frac{\Gamma}{2 \pi r} (1 - e^{-1.26 r^2/r_c^2}) \quad (6)$$

and we shall return to this expression later on in our discussion of real vortices in Section 3.1.

Figure 3 shows the radial vorticity distribution for a generic Gaussian vortex filament as it evolves over time. The series of curves corresponds to a progression of successive instances, showing qualitatively how the vorticity peak decreases, and the core radius increases, with time. Figure 4 shows the corresponding radial distributions of the swirling velocity induced by the generic filament at those same progressive instances in time.

The following two key features of the Gaussian-core model enable its use for accurate representation of the underlying physics:

1. The Gaussian distribution of vorticity enables the representation of the natural viscous decay of the vortex filaments. This allows the freeing up of the memory from vortices that have significantly "dissipated" or "aged".
2. The Gaussian distribution also avoids the mutual high-speed satellization of vortex filaments in close proximity, thereby avoiding unrealistically high tangential velocities. This ensures the stability of the vortex lattice, which enables it to be extended to a large distance downstream from the rotor.

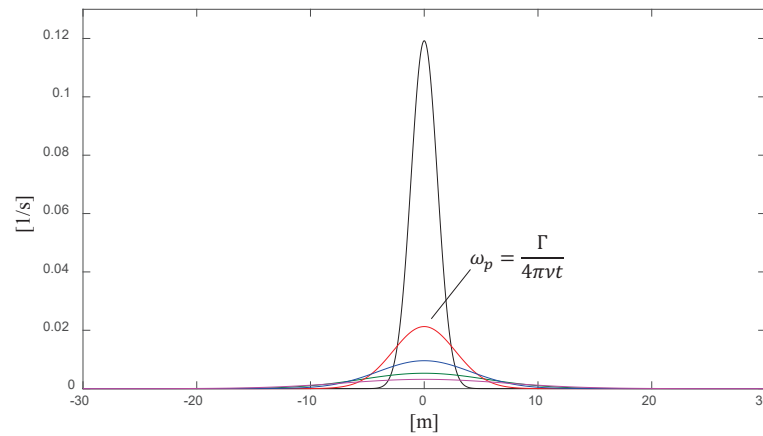


Figure 3. Radial distribution of vorticity for a generic Gaussian vortex filament. The progression of curves shows, qualitatively, how the vorticity evolves with time.

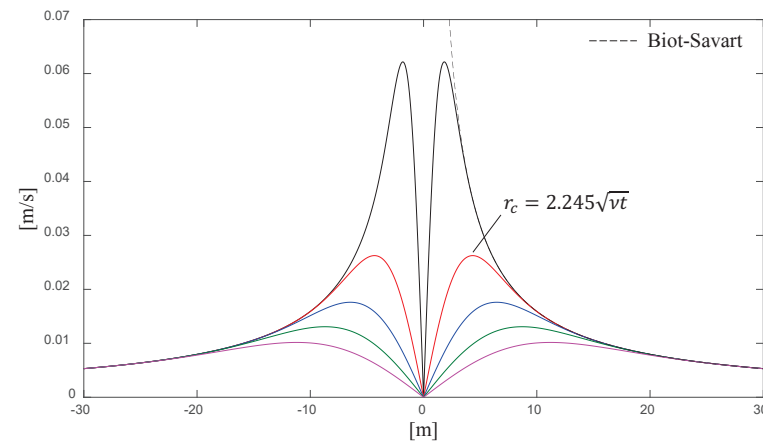


Figure 4. Radial distributions of swirling velocity induced by the generic Gaussian filament shown in Figure 3, at the same progressive instances in time.

As proved in Ponta [29] with this Gaussian distribution of vorticity, the viscous core expands due to diffusion, thereby resulting in a better representation of the vortex evolution process. Ponta [29] also provides a comparison between the direct numerical simulation and experimental data of the effect of viscosity on the vorticity distribution and its rate of decay in a Karman vortex street behind a circular cylinder. By decomposing the incompressible velocity field in the frame of reference of the cylinder into its solenoidal and harmonic components (see also Ponta [34] and Ponta and Aref [35]), Ponta [29] identifies the conditions at which a stable vortex core is reached. It is then demonstrated that, after the stability condition is achieved, the vortex cores exhibit a Gaussian profile for their vorticity distribution, and, from then on, it follows the Lamb-vortex solution.

As we shall discuss in the next section, the determination and proper modeling of the equivalent core radius r_c , at the moment when the vortex core becomes stable, is particularly useful in the development of vortex lattice methods. This is because it ensures a realistic representation of the process of vortex filament creation and further decay, and the subsequent interaction of vortex filaments within the lattice assembly. This constitutes the basis of the GVLM technique described here.

3.1. Core Radius at the Formation of Real Vortices

From Equation (3), it can be seen that, if the time of the creation of the vortex filament is set to zero, the Gaussian distribution of vorticity becomes a Delta function. That is, vorticity at its center is essentially a singularity, and the vortex filament represents a vortex

tube of finite circulation, with infinitesimal thickness and infinite vorticity at its center. This leads to unrealistically high swirling velocities at the early vortex stages, which essentially resembles the Biot–Savart law. That is, even though the Gaussian model is still realistic in its representation of the vortex decay process and its induced velocities in later stages of the vortex’s life, this Delta distribution of vorticity in its initial stage will lead to the same unrealistically extreme velocities in the immediate vicinity of the vortex core that are observed in the Biot–Savart model. This will ultimately create the same problems of chaotic wake instability and wake pattern misrepresentation that we have discussed before.

In reality, vortices in the wake of an object do not emerge as singularities in the Biot–Savart sense. They are created by the rolling up of free shear layers [36,37] and the progressive homogenization of the vorticity radial distribution until a stable vortex core emerges [34,35]. In order to address this loophole in the Lamb-Vortex Model, the authors introduced a finite value for the equivalent core radius at the moment of creation of the *real* vortex (i.e., at $t_{real} = 0$). In terms of the r_c parameter defined in Equation (4), this means that

$$r_c(t_{real}=0) = R_{VorCre}. \quad (7)$$

This notion of R_{VorCre} is one of the fundamental distinctions of the GVLM, and its implementations are based on an extensive series of research work performed in the past, where the process of vortex creation and shedding is analyzed in detail [29,34,35]).

Ponta [29] demonstrated that, in the context of the Lamb-Vortex Model, the notion that vortices have a finite value of the core radius r_c at the moment when they are created (instead of infinitesimal, as in the original Lamb formulation), is the equivalent of assuming that there exists a hypothetical time of vortex creation, t_{VorCre} . This is, essentially, the time that it would take for a Lamb-vortex core to expand until the value of its r_c becomes equivalent to R_{VorCre} .

It is important to notice that the value of t_{VorCre} is not identical to the time taken by the actual process of vortex creation (i.e., the time during which the actual rolling up of the free shear layers occurs until a stable vortex core emerges). It is, instead, the time by which the Lamb-vortex solution should be shifted in order to properly reproduce the actual core size at which a vortex is created in the real process of the shear layer rolling up. We can obtain t_{VorCre} in terms of Equation (4) as

$$R_{VorCre}^2 = r_c^2(t_{real}=0) = 5.04 \nu t_{VorCre} \quad \Rightarrow \quad t_{VorCre} = \frac{R_{VorCre}^2}{5.04 \nu}. \quad (8)$$

From this, we obtain an alternative expression for the value of r_c , now as a function of the corrected time, t_{real} , counted from the moment of creation of a *real* vortex with a core of the finite radius

$$r_c^2(t_{real}) = 5.04 \nu (t_{real} + t_{VorCre}) \quad (9)$$

Then, substituting Equation (8) into Equation (9)

$$r_c^2(t_{real}) = 5.04 \nu t_{real} + R_{VorCre}^2. \quad (10)$$

Now, substituting Equation (10) into Equation (6), an expression for the radial distribution of the swirling velocity induced by a *real* Gaussian vortex can be obtained

$$V(r, t_{real}) = \frac{\Gamma}{2\pi r} (1 - e^{-r^2/(4\nu t_{real} + R_{VorCre}^2/1.26)}). \quad (11)$$

In the context of wind turbine rotor analysis, we currently define R_{VorCre} on a scaling of the thickness of the airfoil section of the blade element that corresponds to a particular vortex filament (see the discussion on vortex lattice creation in Section 3.4). This relates the geometrical size of the vortex core with the characteristic size of the body that produces it. The scaling of R_{VorCre} was finally calibrated by comparing the GVLM results with LiDAR measurements of the wake velocity patterns obtained at Sandia National Lab’s SWIFT

facility in Lubbock, TX, for the test-case scenarios reported in Herges et al. [38] (see also Section 4.2). In this manner, R_{VorCre} provides a realistic approach to the actual radius of the vortex core at the moment when the vortex-formation process is finished and the vortex is shed from the blade section.

3.2. Turbulent Diffusivity Coefficient

In addition to this unique implementation of R_{VorCre} , there is a need to augment the molecular viscosity that appears in the formulas of the original Lamb-Vortex Model, which is defined in the context of purely laminar flow, to account for the additional diffusivity of the turbulent flow. This parameter is essentially an analog to the so-called “eddy viscosity” in typical turbulence-model implementations, such as k- ϵ or LES, but, in this case, applied in the context of a Gaussian vortex lattice model. To this end, we introduce a parameter called the Vortex Turbulent Diffusivity coefficient, ν_{VTD} , as a replacement for the laminar viscosity ν in the original Lamb formulas (i.e., Equations (2) through (4)). The ν_{VTD} coefficient controls the diffusion process, which affects both the rate of expansion of the vortex core and the rate of decay of the peak vorticity at the center of the vortex filament.

Very much akin to the k- ϵ model, it can be seen that the current Gaussian-core implementation involves two calibration parameters: the vortex filament’s equivalent core radius at the time of creation, R_{VorCre} , and the vortex turbulent diffusivity coefficient, ν_{VTD} . These parameters are based on the wind turbine blade, the operational conditions, and the inflow inputs to the model. Of particular care is the choice of ν_{VTD} since it must also consider the inflow inputs—specifically, how the inflow turbulence is introduced in the model. This can be thought to be similar to the modeled and resolved scales of turbulence for contemporary LES codes. The value of ν_{VTD} was calibrated by comparing the GVLM results with LiDAR measurements of the wake velocity patterns, in the same manner described before for R_{VorCre} .

When the ν_{VTD} parameter described above is incorporated into Equation (11), the magnitude of the radial distribution of the swirling velocity induced by a *real* Gaussian filament in turbulent conditions becomes

$$V(r, t_{real}) = \frac{\Gamma}{2\pi r} (1 - e^{-r^2/(4\nu_{VTD} t_{real} + R_{VorCre}^2/1.26)}). \quad (12)$$

Finally, when this induced velocity distribution is applied to a vortex filament of a finite length, as discussed in Figure 2 and Equation (1), the velocity induced by each individual filament in the lattice at a generic point P in its surroundings is given by

$$\mathbf{V}_{ind}^P = \mathbf{e} \frac{\Gamma}{4\pi h} (1 - e^{-h^2/(4\nu_{VTD} t_{real} + R_{VorCre}^2/1.26)}) (\cos \Theta_1 + \cos \Theta_2). \quad (13)$$

3.3. Vortex Transport and Stretching

The Lagrangian markers of the vortex filaments (i.e., the “nodes” of the vortex lattice), are advected through the flow field, which causes strain in the vortex filaments. The stretching (or contraction) of the vortex filaments, in turn, modifies the vortex filament core and, ultimately, the induced velocities. Since the flow is incompressible, the net circulation of any filament remains constant. In the current implementation, the vorticity is assumed to be concentrated inside a corresponding cylinder of its viscous core radius, and the length is assumed to be equal to the length of the filament. The conservation of this filament “volume” provides the change in the radius due to the change in the length of the filament. This modified core radius is then used to compute the induced velocities by the stretched vortex filaments.

The lattice nodes are advected by their local flow velocity. This velocity is the vector sum of the wind-free stream velocity (including any fluctuations present in the atmospheric flow), \mathbf{U}_{wind} , plus the velocity induced at each node by the vortex lattice assembly as a whole, \mathbf{U}_{VorLat} as follows

$$\mathbf{U}_{node} = \mathbf{U}_{wind} + \mathbf{U}_{VorLat} \quad (14)$$

where \mathbf{U}_{VorLat} for each node is obtained as the result of the velocity induced at its location by the addition of the velocities induced by all of the individual filaments in the entire lattice assembly, \mathbf{V}_{ind} , as given by Equation (13).

The advected positions of the filament nodes are obtained from the second-order explicit Adams–Bashforth (AB2) time integration:

$$\Delta \mathbf{X}_{node} = \left[\frac{3}{2}(\mathbf{U}_{node})^{t_{curr}} - \frac{1}{2}(\mathbf{U}_{node})^{t_{prev}} \right] \Delta t \quad (15)$$

where t_{curr} and t_{prev} are, respectively, the indexes of the current and the previous steps in the time-solution iterative process.

Being an “open” method, the AB2 scheme offers an acceptable trade-off between stability, accuracy, and computational cost. Hence, it is suitable for the simulation of the vortex wakes of multiple wind turbines in a wind farm.

3.4. Computation of the Circulation of Vortex Filaments and Vortex Lattice Creation

The GVLM combined with CODEF’s blade structural and rotor flow models leads to highly accurate farm simulations when compared to traditional BEM-based codes but at significantly reduced computational costs when compared to DNS/LES codes. The general approach of a vortex lattice technique involves the division of the wind turbine blade into a number of segments (commonly referred to as *blade elements*) along their span (for more details, see Strickland et al. [24] and Ponta and Jacovkis [25]). Each blade element is represented by a *Bound* vortex filament. In the context of free vortex lattice models, the use of a single Bound vortex filament is commonly accepted to adequately represent the blade-element flow field at distances equal to or greater than one chord length from the airfoil blade section, which is sufficient for the purposes of these methods.

The circulation of this Bound vortex filament, Γ_{Bn} , is obtained via the Kutta–Joukowski theorem. At each time step, the DRD-BEM provides an accurate computation of the relative velocity of the flow incident on each blade section. This provides the velocity magnitude of the incident flow and its angle of attack, α , which consequently provides the value of its aerodynamic coefficients. Using the Kutta–Joukowski theorem, we obtain Γ_{Bn} as

$$\Gamma_{Bn} = \frac{1}{2} U_{rel} C_l c \quad (16)$$

where U_{rel} is the magnitude of the relative velocity of the incident flow for the airfoil section, C_l is the lift coefficient, and c is the airfoil section chord.

In order to satisfy Helmholtz’s Theorem [30], a *Trailing* filament is created at the boundary between two blade-elements. The circulation of each Trailing filament has to be equal to the difference between the circulation of its two adjacent Bound filaments at the moment when the Trailing filament emerges. On the other hand, in order to satisfy Kelvin’s Theorem [30], a *Shed* filament emerges from each blade-element at every time step. The circulation of each Shed filament has to be equal to the difference between the circulation of its corresponding Bound filament at the current instance in time and at the previous instance. Figure 5 shows a schematic of the construction of a vortex lattice consisting of an assembly of Bound, Shed, and Trailing filaments for a generic wind turbine blade. Following the principles stated above, the circulations of the Shed and Trailing filaments associated with the current time step t_i are obtained as follows:

$$\Gamma_{Sh_i}^{j-1} = \Gamma_{Bn_i}^{j-1} - \Gamma_{Bn_i'}^j \quad (17)$$

$$\Gamma_{Tr_i}^{j-1} = \Gamma_{Bn_i}^j - \Gamma_{Bn_{i-1}}^j \quad (18)$$

At every time step, the induced velocity for each filament node is obtained by obtaining the induction from all of the other filaments of the vortex lattice. In this manner, a system of Shed and Trailing vortex filaments is created and advected.

This implies that as the vortex shedding process progresses, the vortex lattice extends with time. This leads to an increase in the computational time per time step. We manage this increase in several ways that will be discussed in the following subsections.

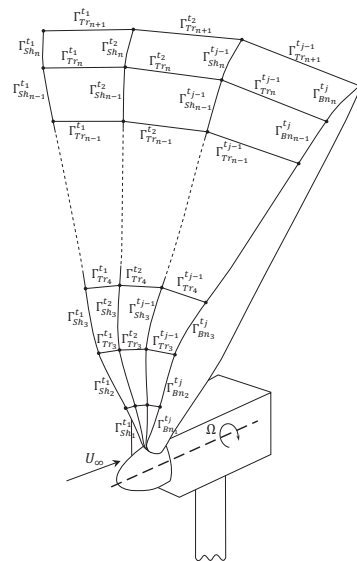


Figure 5. A schematic showing the Bound, Trailing, and Shed vortex filaments in the construction of a lattice assembly of a generic wind turbine blade.

3.5. Lattice Wake Growth

In the current implementation of the GVLM, the time step of the aeroelastic solver, the DRD-BEM, and the vortex wake module, the GVLMs are different but coupled. The method retains the capability of shedding a vortex filament system at every aeroelastic time step, but such small time steps could lead to a vortex lattice with a large number of filaments. For the purpose of studying the wake of the turbine and its interaction with other turbines in the farm, such large vortex lattice ensembles are superfluous and render the method computationally prohibitive. Furthermore, the scales of the vortex dynamics phenomena of interest do not necessitate such numerous steps. Small-scale phenomena can be represented very effectively through model parameters such as ν_{VTD} , akin to the sub-grid scale modeling in LES. Hence, having different time steps effectively compartmentalizes the two different, yet closely related, aspects of the overall simulation. Currently, the vortex shedding process takes place upon completion of a certain number of DRD-BEM steps. This relationship can be implicitly or explicitly specified as inputs to the solver.

Since the GVLM is a Lagrangian method, the flow domain is essentially infinite. The lattice nodes are added to the lattice by the physical process of vortex generation itself and follow the fundamental features of the vortex wake in its evolution in a self-advecting manner, similar to a naturally adaptive mesh. This means that nodes are only added to the solution when and where they are necessary, making the vortex lattice methods extremely efficient from the computational point of view.

The choice of the maximum lattice size is a balance of the domain required for an appropriate/acceptable description of the vortex wake and the computational expense incurred. Some of the factors considered in arriving at this size limit include the age and distance downstream of the filaments at the tale of the lattice, which, after a certain level of decay, lose any influence in terms of their capacity to induce velocity and become irrelevant. At this point, those filaments can be deleted for memory and to save computational resources. The determinant factors to establish that cap are the operating conditions, including the input wind speed and level of turbulence (which affects turbulent diffusivity and, hence, the rate of vortex decay), the turbine's operational parameters, and the relative location of the vortex wake filaments.

In the current implementation of the GVLM, the growth of the lattice is capped at a certain number of shedding events. This number can be implicitly or explicitly specified as an input, depending on the determinant factors mentioned above. Beyond this cap number, the older vortex filaments are deleted and replaced by new ones, keeping the number of data in memory constant.

4. Numerical Experiments and Analysis of Results

In this section, we shall discuss the numerical study conducted with the newly expanded CODEF suite. We begin with the initial verification of the GVLM for a single turbine. This is followed by a comparison with field measurements as part of our association with Sandia National Laboratories (SNL).

4.1. Validation Simulations with the NREL N5M-Reference Wind Turbine

The primary goal of this phase of the numerical study was to ensure the stability of the vortex lattice code and its interface with the existing DRD-BEM/GTBM modules. The NREL N5M-Reference Wind Turbine (N5M-RWT), presented in Jonkman et al. [22], designed for onshore as well as offshore installations, is still considered a good representation of the state-of-the-art, utility-scale, multi-megawatt commercial turbines. Initial simulations in this phase were conducted with the N5M-RWT operating in a uniform wind stream at its nominal design conditions of 11.4 m/s and 12.1 rpm. As an example, Figure 6 shows the complete vortex lattice of the N5M-RWT at its nominal, steady-state conditions. We can see the regularity in the vortex lattice extend far downstream ($\sim 15D$) of the turbine. This verified that the GVLM implementation was stable, and, if continued for a longer time, the vortex lattice would also steadily grow without any problems of convergence or singularity-driven, infinite-velocity advection.

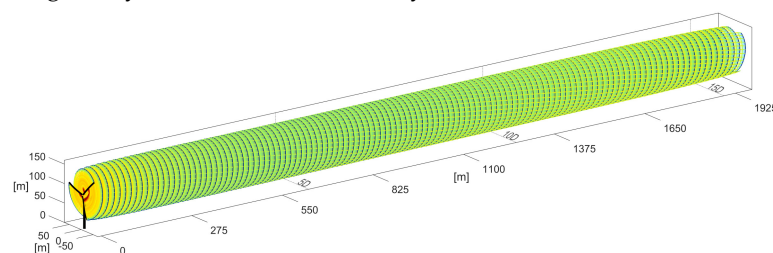


Figure 6. The complete, stable vortex lattice of the N5M-RWT extending more than $15D$ downstream of the turbine in steady-state flow, at its nominal operational conditions.

4.2. Numerical Experiments on SNL's SWiFT Facility Scenarios

The numerical experiments involved simulations representative of the wind turbines at SNL's Scaled Wind Farm Technology (SWiFT) facility, as described in Berg et al. [39]. The SWiFT facility is very unique with its vast number of in situ measurements, which are publicly available to verify, validate, and tune computational models. Future plans at the site involving extensive wind turbine wake and waked rotor blade measurements shall further enrich the development of computational models.

4.3. SWiFT Facility Overview

Located in Lubbock, TX, USA, SNL's SWiFT facility consists of three modified Vestas V27 variable-speed, variable-pitch turbines rated at 225 kW (Vestas, Aarhus, Denmark) and two 60 m anemometry towers. The facility has been designed to support investigations to reduce the turbine-to-turbine interactions and enhance wind farm performance. It has also been used for the development and testing of novel wind turbine rotors.

The facility consists of heavily instrumented anemometry towers and wind turbines with a suite of sensors. Figure 7 shows the layout of the SWiFT site.



Figure 7. Layout of SNL's SWiFT site in Lubbock, TX, USA.

With over 2 years of historical data, reported by Kelley and Ennis [40], the atmospheric conditions are well characterized, especially at scales important for wind power. The site is located in the flat Texas Panhandle with a consistent wind from the south (average 180.5° N).

The two met towers are placed 2.5 rotor diameters upwind of the wind turbines. The three turbines are placed in a right-triangular layout. Two turbines (WTGa1 and WTGb1) are placed side-by-side, three rotor diameters apart, and the third turbine (WTGa2) is placed five rotor diameters downwind of WTGa1.

Of the numerous sensors and instrumentation on the met towers and turbines, the following are of particular interest to us:

1. The cup anemometers at three different heights on the met tower;
2. The 3D sonic anemometers at five different heights of the met tower;
3. The yaw measurement sensor on the turbines;
4. The DTU Spinner LiDAR located in the nacelle of turbine WTGa1.

The Vestas V27 turbine is based on design philosophies belonging to the generation of turbines represented by the N5M-RWT. We conducted our vortex wake simulations using a version of the N5M-RWT scaled down (herein referred to as the *N5M27*) to the V27 turbine at three different inflow conditions, as reported in Herges et al. [38].

The values of the different parameters of inflow conditions are 10 min averages of the anemometry measurements. Table 1 summarizes the three different scenarios reported by Herges et al. [38], which we used as inputs for the CODEF simulations.

The inclusion of these parameters in the inflow enabled the comparison of the CODEF simulations to the LiDAR measurement cases reported in Herges et al. [38]. The CODEF line-of-sight velocity, v_{los} , is computed at the same distance downwind as that of the LiDAR. These v_{los} data can be obtained with no restrictions to the grid spacing. In this post-processing step, in addition to the v_{los} , we can obtain the individual components of the wake-induced velocities superimposed on the inflow wind. Thus, CODEF can easily and accurately provide the velocity field anywhere in the domain being considered.

Table 1. Flow parameters corresponding to the three scenarios reported by Herges et al. [38] used as inputs for the CODEF simulations. Figures 7, 9, and 11 labels accompanying each Scenario correspond to the figures in which the respective scenario is reported in Herges et al. [38].

Scenario (Fig. No in [38])	Wind Speed [m/s]	Alpha	Veer [deg]	Yaw Offset [deg]
Scenario 1 (Fig. 7)	8.2	0.12	1.3°	5.9°
Scenario 2 (Fig. 9)	6.9	0.37	14.6°	-0.12°
Scenario 3 (Fig. 11)	4.8	0.15	-5.0°	10.9°

The first set of our simulation studies based on the field measurements that represented the operation conditions of the SWiFT turbines demonstrates the complex evolution of the vortex wake, in realistic wind input conditions based on field anemometry measurements. Figure 8 shows a perspective view of the GVLM vortex lattice wake extending five diameters downstream of the turbine, computed for the conditions of Scenario 1 listed in Table 1. The color scheme used in Figure 8, and in all subsequent vortex lattice images in this section, is intended to provide a better perspective to appreciate the vortex lattice shape development in space and is not attached to a specific physical quantity.

The dynamics of the wake can be better appreciated when we consider cross-cut section views of the lattice structure at several downstream locations. Figure 9 shows rear views of the lattice cross-cut sections at six different locations downstream of the turbine, for the conditions of Scenario 1.

The filaments represented by this lattice were used to obtain the line-of-sight velocity akin to that measured by the LiDAR located in the SWiFT turbine's nacelle. The v_{los} was obtained at the same surfaces located downstream of the turbine as reported in Herges et al. [38]. Figure 10 shows the LiDAR measurements of v_{los} patterns at six different distances located from one to five diameters downstream of the turbine for the conditions of Scenario 1 (as reported in Figure 7 of Herges et al. [38]), and Figure 11 shows the corresponding GVLM results at the same locations. Figures 10 and 11 are provided with an identical color scale for the velocity contours, in this manner, a quantitative comparison of velocity values between the experimental and the numerical results is possible. The same is completed for all other subsequent figures showing velocity pattern comparisons.

We also conducted simulations for Scenarios 2 and 3 of Table 1. Figure 12 shows a perspective view of the GVLM vortex lattice wake for Scenario 2, and Figure 13 shows the vortex lattice cross-cut sections at five different locations downstream of the turbine. Figure 14 shows the LiDAR measurements of v_{los} patterns at five different distances located from 1 to 5 diameters downstream of the turbine for the conditions of Scenario 2 (as reported in Figure 9 of Herges et al. [38]), and Figure 15 shows the corresponding GVLM results. Figure 16 shows a perspective view of the GVLM vortex lattice wake for Scenario 3, and Figure 17 shows the vortex lattice cross-cut sections. Finally, Figure 18 shows the LiDAR measurements of the v_{los} patterns for the conditions of Scenario 3 (as reported in Figure 11 of Herges et al. [38]), and Figure 19 shows the corresponding GVLM results.

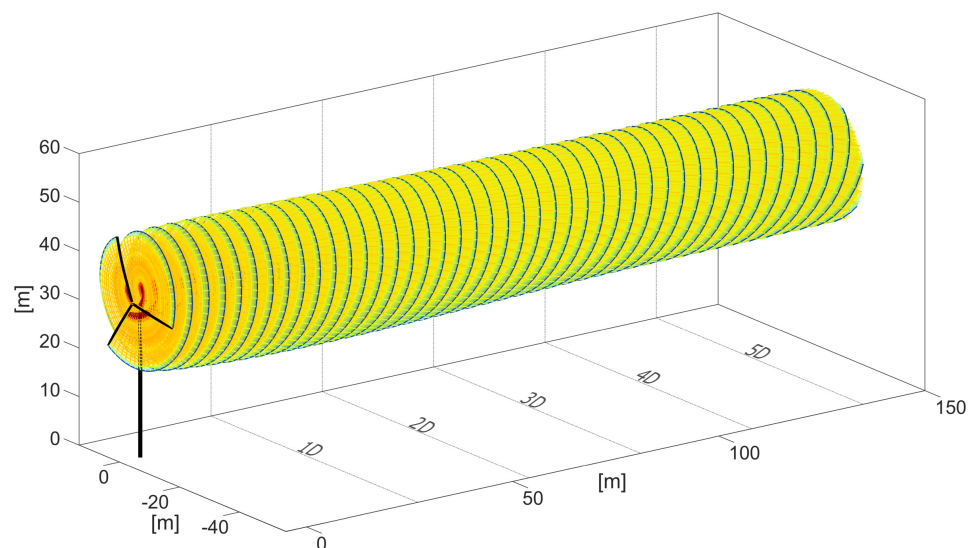


Figure 8. Perspective view of the GVLM vortex lattice wake for Scenario 1. The color scheme used in all vortex lattice images is intended to provide a better appreciation of the lattice shape development and is not attached to a specific physical quantity.

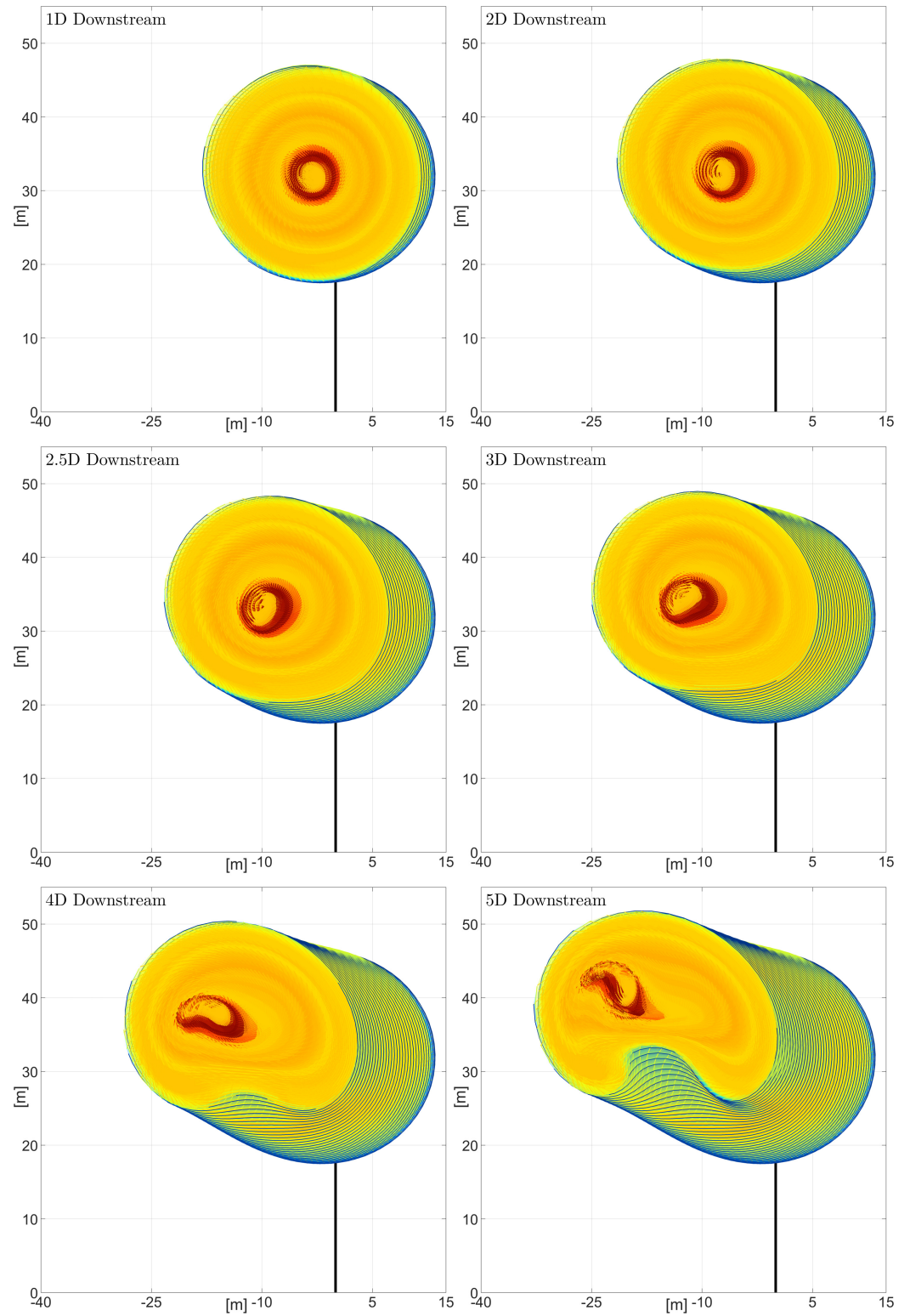


Figure 9. Rear views of the lattice cross-cut sections at six different locations downstream of the turbine for Scenario 1.

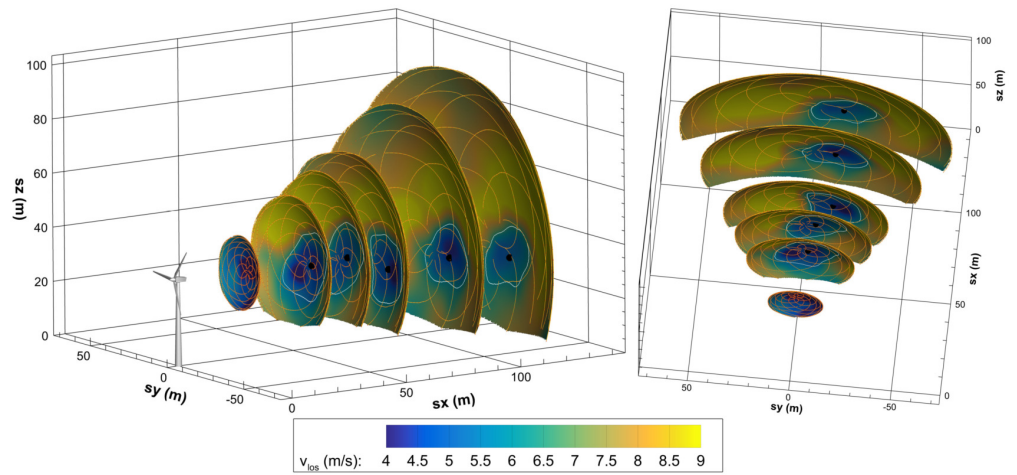


Figure 10. LiDAR measurements of v_{los} patterns at six different distances located from 1 to 5 diameters downstream of the turbine for Scenario 1, as reported in Figure 7 of Herges et al. [38].

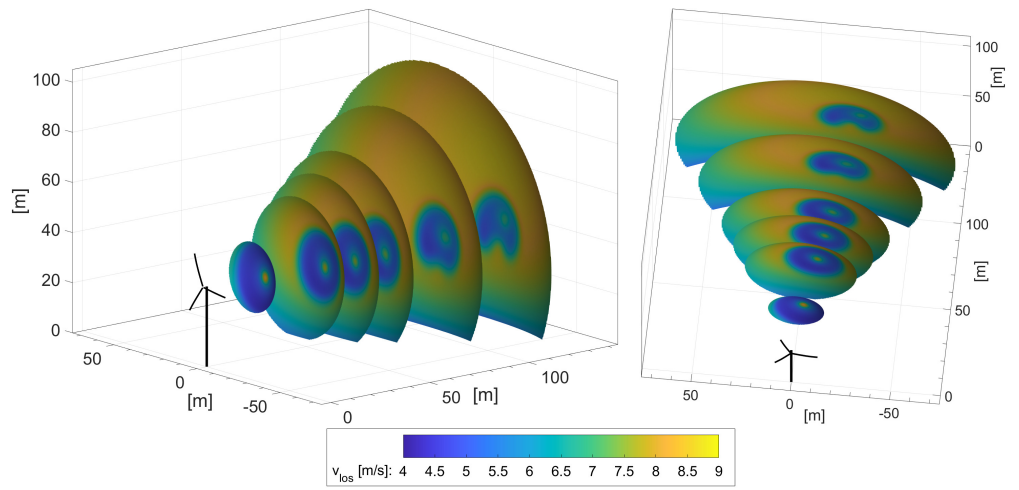


Figure 11. GVLM results for the v_{los} patterns in Scenario 1 at the same downstream locations shown in Figure 10.

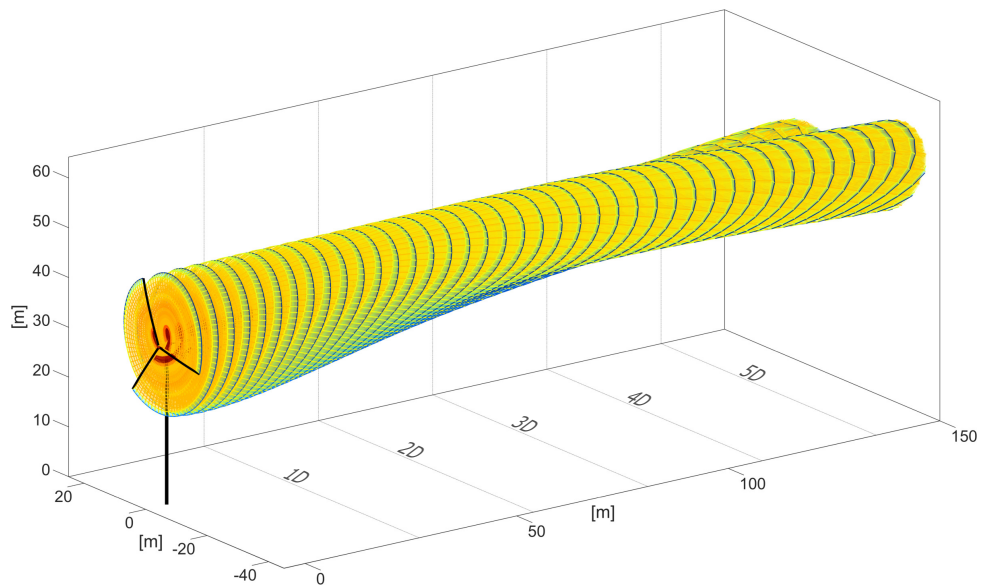


Figure 12. Perspective view of the GVLM vortex lattice wake for Scenario 2.

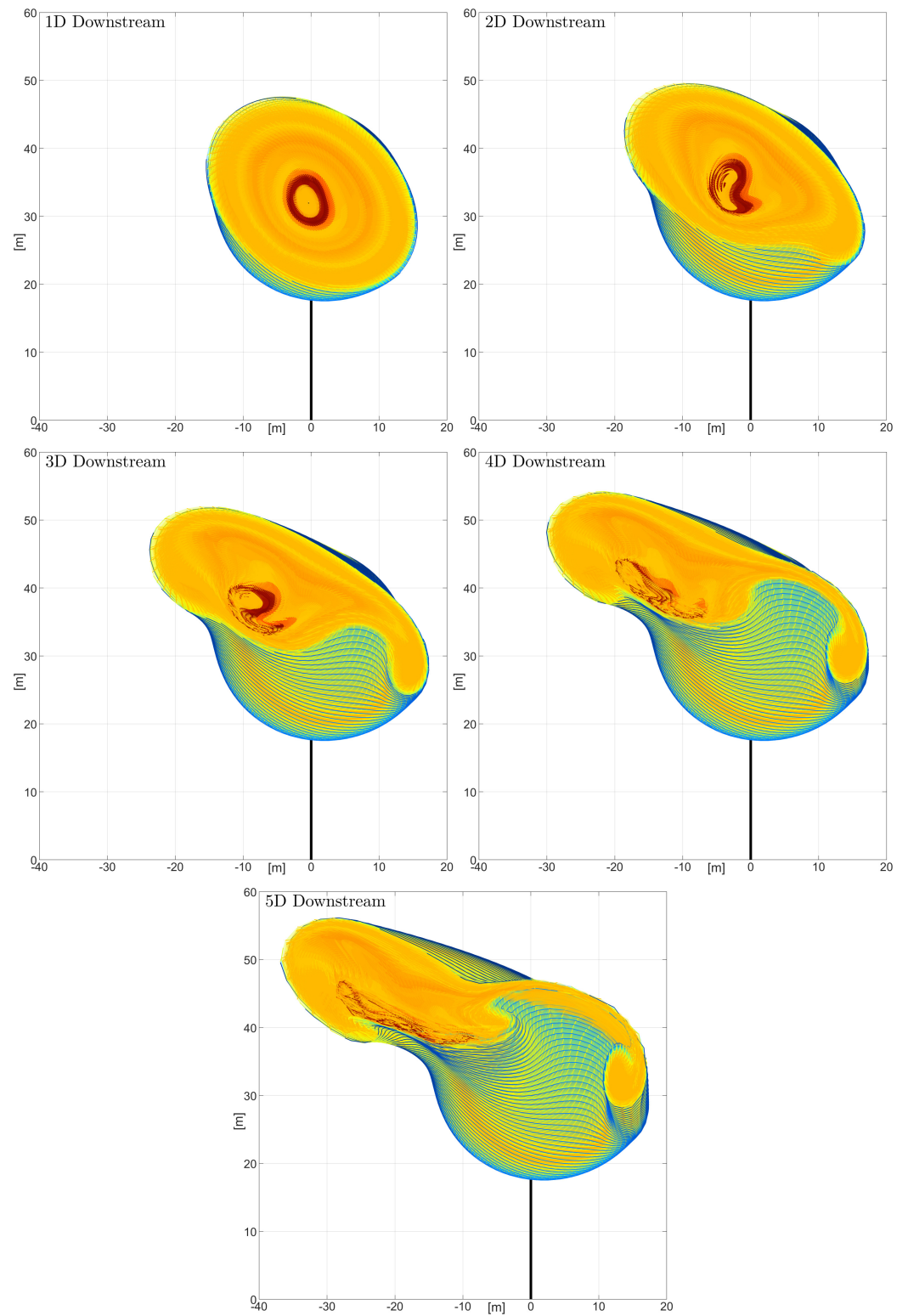


Figure 13. Rear views of the lattice cross-cut sections at five different locations downstream of the turbine for Scenario 2.

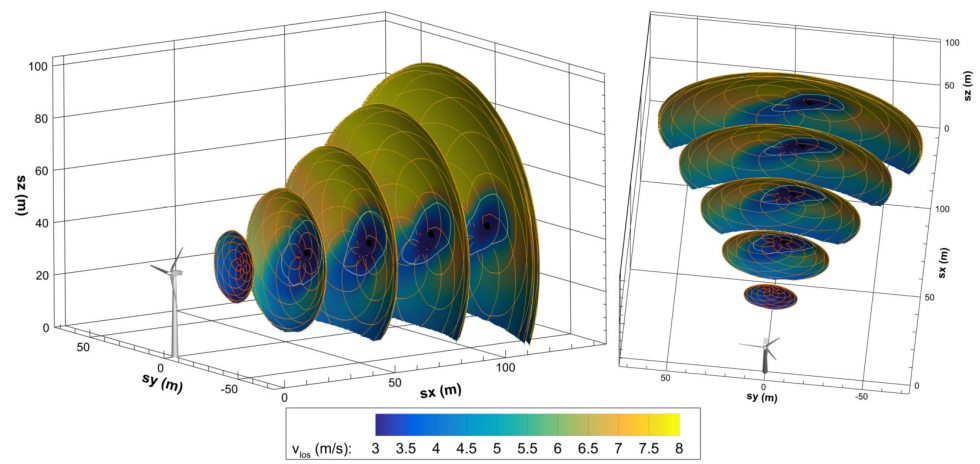


Figure 14. LiDAR measurements of v_{los} patterns at five different distances located from 1 to 5 diameters downstream of the turbine for Scenario 2, as reported in Figure 9 of Herges et al. [38].

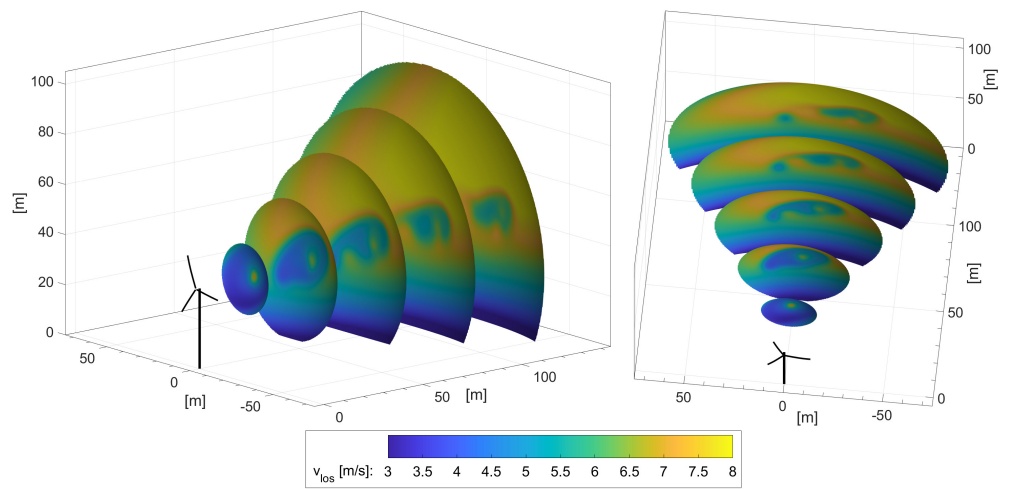


Figure 15. GVLM results for the v_{los} patterns in Scenario 2 at the same downstream locations shown in Figure 14.

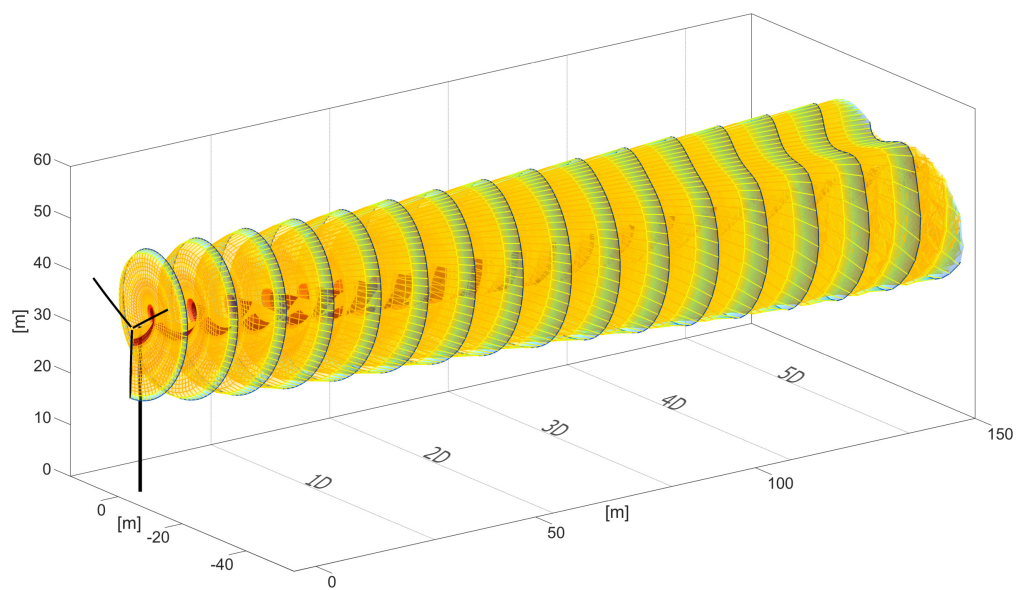


Figure 16. Perspective view of the GVLM vortex lattice wake for Scenario 3.

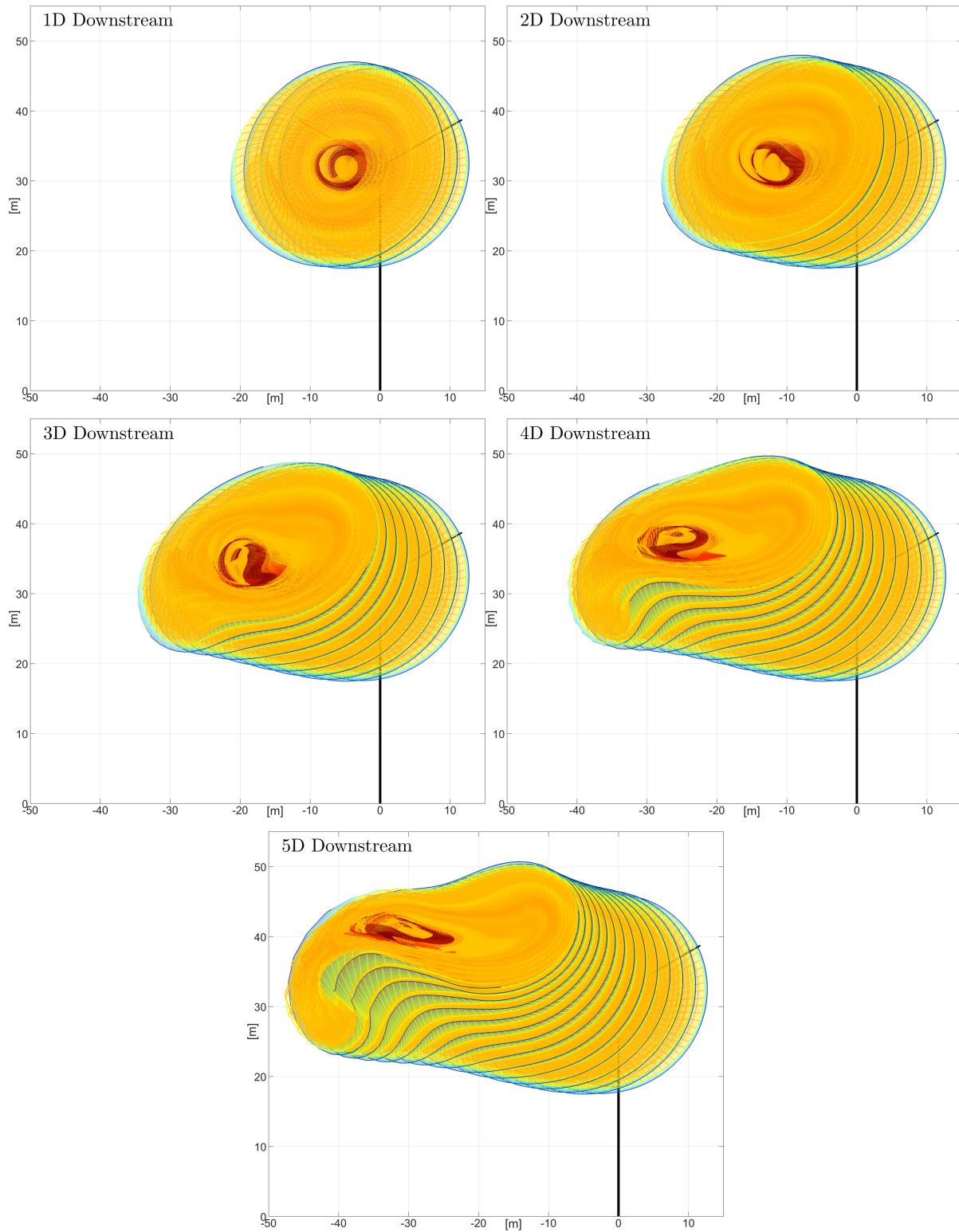


Figure 17. Rear views of the lattice cross-cut sections at five different locations downstream of the turbine for Scenario 3.

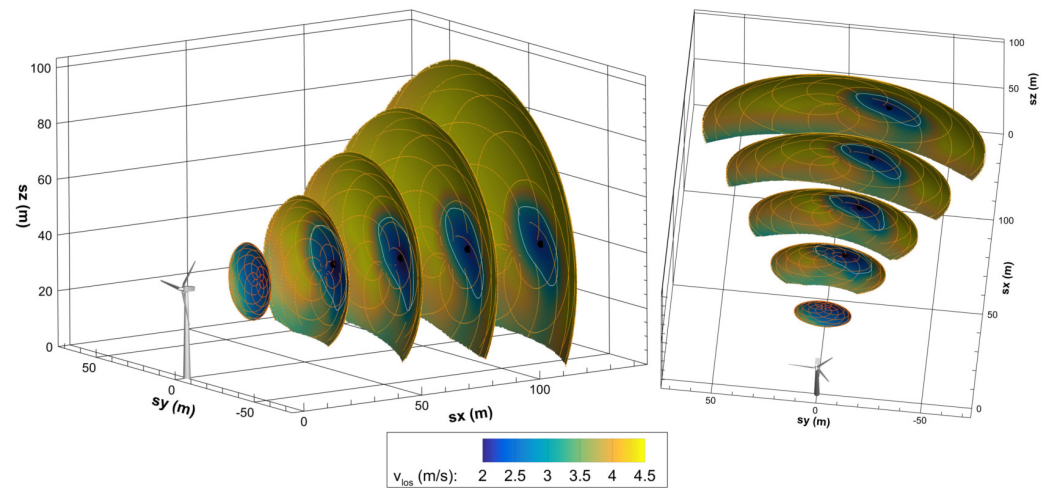


Figure 18. LiDAR measurements of v_{los} patterns at five different distances located from 1 to 5 diameters downstream of the turbine for Scenario 3, as reported in Figure 11 of Herges et al. [38].

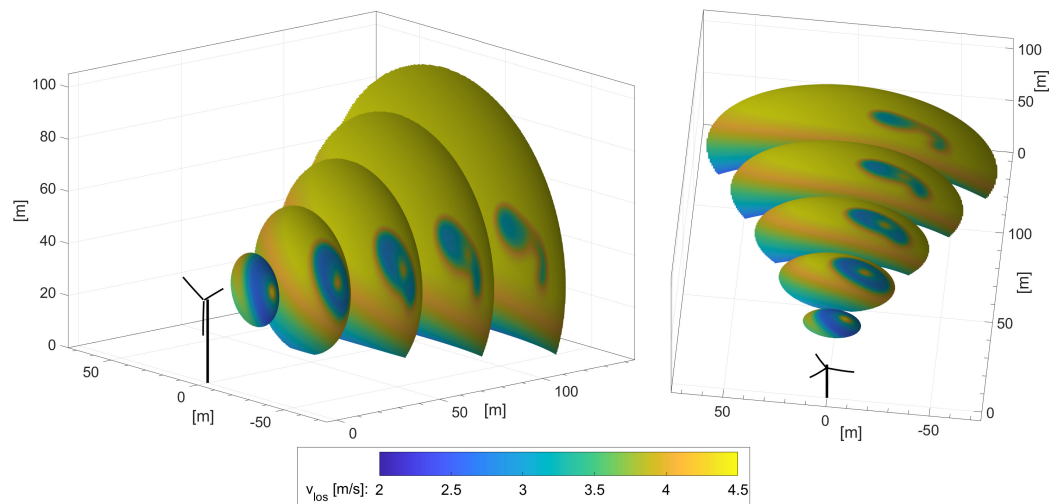


Figure 19. GVLM results for the v_{los} patterns in Scenario 3 at the same downstream locations shown in Figure 18.

5. Conclusions and Outlook for Future Work

Through the endeavor presented here, we have seen the successful integration of the Gaussian-core Vortex Lattice Model (GVLM) with the high-fidelity aeroelastic routines of the DRD-BEM/GTBM modules, thereby expanding the capabilities of the CODEF multi-physics suite.

The stability of the model was demonstrated for the N5M-RWT with a vortex wake extending more than 15D downstream. This initial model validation paved the way for simulations with complex inflows and comparisons with field measurements.

The simulations of the SNL-SWiFT turbines showcase the model's responsiveness to the varying inflow parameters. The current GVLM implementation involves the use of the same flow details obtained from the met tower (or as experienced at the turbine) to compute the propagation of every filament node of all lattices. Despite this approach, there are remarkable qualitative and quantitative similarities in terms of the magnitude of the velocity patterns and the location and shape of the spots of velocity deficit between the GVLM-computed v_{los} and its LiDAR-measured counterpart. This demonstrates the GVLM's capabilities for accurately capturing the complex evolution of the vortex wake and the highly dynamic wake-to-wake interaction. Such similarities in the absence of any spatially varying transient wind flow inputs reinforce the strength of the model and its

responsiveness to the calibration parameters. Hence, even in its current form, the model can be extremely useful for quick, moderately high-fidelity engineering design stages involving wind turbine wakes.

The current model is stable to run farms comprised multiple wind turbines using computational hardware that is available at a mere fraction of the cost (human, capital, and operational) of contemporary LES without significantly compromising its fidelity/results.

The vortex wake implementation is devoid of any singularities/computational irregularities. The current model is stable to run multiple turbines in a wind farm and capture the complex turbine-to-turbine vortex wake interactions. The addition of the transient wind flow information over the entire region of a wind farm shall enable accurate quantitative comparisons with the LiDAR wake measurements. These future efforts position CODEF to be well suited for high-fidelity wind farm simulations that incorporate farm-collective and electric microgrid control strategies to optimize the overall output.

Author Contributions: Conceptualization, A.B. and F.P.; methodology, A.B. and F.P.; software, A.B. and F.P.; validation, A.B. and F.P.; formal analysis, A.B. and F.P.; investigation, A.B. and F.P.; resources, A.B. and F.P.; data curation, A.B. and F.P.; writing—original draft preparation, A.B. and F.P.; writing—review and editing, A.B. and F.P.; visualization, A.B. and F.P.; supervision, F.P.; project administration, F.P.; funding acquisition, F.P. All authors have read and agreed to the published version of the manuscript.

Funding: The authors gratefully acknowledge the financial support of Sandia National Labs, USA, through awards PO-2074866 and PO-2159403, and the ME-EM Department at Michigan Technological University.

Data Availability Statement: Data are contained within the article.

Conflicts of Interest: The authors declare no conflict of interest.

References

1. IRENA. *Global Energy Transformation: A Roadmap to 2050 (2019 Edition)*; Technical Report; International Renewable Energy Agency: Abu Dhabi, United Arab Emirates, 2019.
2. Dykes, K.L.; Veers, P.S.; Lantz, E.J.; Holttinen, H.; Carlson, O.; Tuohy, A.; Sempreviva, A.M.; Clifton, A.; Rodrigo, J.S.; Berry, D.S.; et al. *IEA Wind TCP: Results of IEA Wind TCP Workshop on a Grand Vision for Wind Energy Technology*; Technical Report NREL/TP-5000-72437; National Renewable Energy Laboratory: Golden, CO, USA, 2019.
3. Veers, P.; Dykes, K.; Lantz, E.; Barth, S.; Bottasso, C.L.; Carlson, O.; Clifton, A.; Green, J.; Green, P.; Holttinen, H.; et al. Grand challenges in the science of wind energy. *Science* **2019**, *366*, eaau2027. [[CrossRef](#)] [[PubMed](#)]
4. Gebraad, P.M.; Teeuwisse, F.W.; Van Wingerden, J.; Fleming, P.A.; Ruben, S.D.; Marden, J.R.; Pao, L.Y. Wind plant power optimization through yaw control using a parametric model for wake effects—A CFD simulation study. *Wind Energy* **2016**, *19*, 95–114. [[CrossRef](#)]
5. Ekaterinaris, J.A. Numerical simulation of incompressible two-blade rotor flowfields. *J. Propuls. Power* **1998**, *14*, 367–374. [[CrossRef](#)]
6. Duque, E.; Van Dam, C.; Hughes, S. Navier-Stokes simulations of the NREL combined experiment phase II rotor. In Proceedings of the 37th Aerospace Sciences Meeting and Exhibit, Reno, NV, USA, 11–14 January 1999; p. 37.
7. Sorensen, N. Aerodynamic predictions for the unsteady aerodynamics experiment phase-II rotor at the National Renewable Energy Laboratory. In Proceedings of the 2000 ASME Wind Energy Symposium, Reno, NV, USA, 10–13 January 2000; p. 37.
8. Hansen, M.; Sorensen, J.; Michelsen, J.; Sorensen, N.; Hansen, M.; Sorensen, J.; Michelsen, J.; Sorensen, N. A global Navier-Stokes rotor prediction model. In Proceedings of the 35th Aerospace Sciences Meeting and Exhibit, Reno, NV, USA, 6–9 January 1997; p. 970.
9. Maronga, B.; Gryscha, M.; Heinze, R.; Hoffmann, F.; Kanani-Sühring, F.; Keck, M.; Ketelsen, K.; Letzel, M.O.; Sühring, M.; Raasch, S. The Parallelized Large-Eddy Simulation Model (PALM) version 4.0 for atmospheric and oceanic flows: Model formulation, recent developments, and future perspectives. *Geosci. Model Dev.* **2015**, *8*, 2515–2551. [[CrossRef](#)]
10. Churchfield, M.; Lee, S.; Moriarty, P.; Martinez, L.; Leonardi, S.; Vijayakumar, G.; Brasseur, J. A large-eddy simulation of wind-plant aerodynamics. In Proceedings of the 50th AIAA Aerospace Sciences Meeting including the New Horizons Forum and Aerospace Exposition, Nashville, TN, USA, 9–12 January 2012; p. 537.
11. Domino, S. *Sierra Low Mach Module: Nalu Theory Manual 1.0*; Sandia National Laboratories Unclassified Unlimited Release: Albuquerque, NM, USA, 2015.
12. Sprague, M.A.; Ananthan, S.; Vijayakumar, G.; Robinson, M. ExaWind: A multifidelity modeling and simulation environment for wind energy. *J. Phys. Conf. Ser.* **2020**, *1452*, 012071. [[CrossRef](#)]

13. Van Bussel, G.J. The Aerodynamics of Horizontal Axis Wind Turbine Rotors Explored with Asymptotic Expansion Methods. Ph.D. Thesis, Delft University of Technology, Delft, The Netherlands, 1995.
14. Doubrawa, P.; Quon, E.W.; Martinez-Tossas, L.A.; Shaler, K.; Debnath, M.; Hamilton, N.; Herges, T.G.; Maniaci, D.; Kelley, C.L.; Hsieh, A.S.; et al. Multimodel validation of single wakes in neutral and stratified atmospheric conditions. *Wind Energy* **2020**, *23*, 2027–2055. [[CrossRef](#)]
15. Lignarolo, L.E.; Mehta, D.; Stevens, R.J.; Yilmaz, A.E.; van Kuik, G.; Andersen, S.J.; Meneveau, C.; Ferreira, C.J.; Ragni, D.; Meyers, J.; et al. Validation of four LES and a vortex model against stereo-PIV measurements in the near wake of an actuator disc and a wind turbine. *Renew. Energy* **2016**, *94*, 510–523. [[CrossRef](#)]
16. Leishman, J.G. *Principles of Helicopter Aerodynamics*; Cambridge University Press: Cambridge, UK, 2006.
17. Manwell, J.F.; McGowan, J.G.; Rogers, A.L. *Wind Energy Explained: Theory, Design and Application*; Wiley: Chichester, UK, 2009.
18. Burton, T.; Sharpe, D.; Jenkins, N.; Bossanyi, E. *Wind Energy Handbook*; Wiley: Chichester, UK, 2001.
19. Ponta, F.L.; Otero, A.D.; Lago, L.I.; Rajan, A. Effects of rotor deformation in wind-turbine performance: The Dynamic Rotor Deformation Blade Element Momentum model (DRD-BEM). *Renew. Energy* **2016**, *92*, 157–170. [[CrossRef](#)]
20. Hodges, D.H. *Nonlinear Composite Beam Theory*; AIAA: Reston, VA, USA, 2006.
21. Yu, W.; Hodges, D.H.; Volovoi, V.; Cesnik, C.E.S. On Timoshenko-like modeling of initially curved and twisted composite beams. *Int. J. Sol. Struct.* **2002**, *39*, 5101–5121. [[CrossRef](#)]
22. Jonkman, J.; Butterfield, S.; Musial, W.; Scott, G. *Definition of a 5-MW Reference Wind Turbine for Offshore System Development*; Technical Report NREL/TP-500-38060; National Renewable Energy Laboratory: Golden, CO, USA, 2009.
23. Xudong, W.; Shen, W.Z.; Zhu, W.J.; Sorensen, J.; Jin, C. Shape optimization of wind turbine blades. *Wind Energy* **2009**, *12*, 781–803. [[CrossRef](#)]
24. Strickland, J.H.; Webster, B.T.; Nguyen, T. A Vortex Model of the Darrieus Turbine: An Analytical and Experimental Study. *J. Fluids Eng.* **1979**, *101*, 500–505. [[CrossRef](#)]
25. Ponta, F.L.; Jacovkis, P.M. A vortex model for Darrieus turbine using finite element techniques. *Renew. Energy* **2001**, *24*, 1–18. [[CrossRef](#)]
26. Karamcheti, K. *Principles of Ideal-Fluid Aerodynamics*; Wiley: New York, NY, USA, 1966.
27. Cottet, G.H.; Koumoutsakos, P.D. *Vortex Methods: Theory and Practice*; Cambridge University Press: London, UK, 2000.
28. Lamb, H. *Hydrodynamics*, 6th ed.; Cambridge University Press: Cambridge, UK, 1932.
29. Ponta, F.L. Vortex decay in the Kármán eddy street. *Phys. Fluids* **2010**, *22*, 093601. [[CrossRef](#)]
30. Batchelor, G.K. *An Introduction to Fluid Dynamics*; Cambridge University Press: Cambridge, UK, 2000.
31. Hooker, S.G. On the action of viscosity in increasing the spacing ration of a vortex street. *Proc. R. Soc. Lond. Ser. A Math. Phys. Sci.* **1936**, *A154*, 67–89.
32. Flór, J.B.; van Heijst, G.J.F. An experimental study of dipolar structures in a stratified fluid. *J. Fluid Mech.* **1994**, *279*, 101–133. [[CrossRef](#)]
33. Trieling, R.R.; van Wesenbeeck, J.M.A.; van Heijst, G.J.F. Dipolar vortices in a strain flow. *Phys. Fluids* **1998**, *10*, 144–159. [[CrossRef](#)]
34. Ponta, F.L. Analyzing the vortex dynamics in bluff-body wakes by Helmholtz decomposition of the velocity field. *Fluid Dyn. Res.* **2006**, *38*, 431–451. [[CrossRef](#)]
35. Ponta, F.L.; Aref, H. Strouhal-Reynolds number relationship for vortex streets. *Phys. Rev. Lett.* **2004**, *93*, 084501. [[CrossRef](#)] [[PubMed](#)]
36. Kovasznay, L.S.G. Hot-wire investigations of the wake behind cylinders at low Reynolds numbers. *Proc. R. Soc. Lond. Ser. A Math. Phys. Sci.* **1949**, *A198*, 174–190.
37. Zdravkovich, M.M. *Flow Around Circular Cylinders*; Oxford University Press: Oxford, UK, 1997; Volume 1.
38. Herges, T.; Maniaci, D.C.; Naughton, B.T.; Mikkelsen, T.; Sjöholm, M. High resolution wind turbine wake measurements with a scanning lidar. *J. Phys. Conf. Ser.* **2017**, *854*, 012021. [[CrossRef](#)]
39. Berg, J.; Bryant, J.; LeBlanc, B.; Maniaci, D.C.; Naughton, B.; Paquette, J.A.; Resor, B.R.; White, J.; Kroeker, D. Scaled wind farm technology facility overview. In Proceedings of the 32nd ASME Wind Energy Symposium, National Harbor, MD, USA, 13–17 January 2014; p. 1088.
40. Kelley, C.L.; Ennis, B.L. *SWiFT Site Atmospheric Characterization*; Technical Report SAND2016-0216; Sandia National Lab.: Albuquerque, NM, USA, 2016.

Disclaimer/Publisher’s Note: The statements, opinions and data contained in all publications are solely those of the individual author(s) and contributor(s) and not of MDPI and/or the editor(s). MDPI and/or the editor(s) disclaim responsibility for any injury to people or property resulting from any ideas, methods, instructions or products referred to in the content.